Highlights

Limitations of snapshot hyperspectral cameras to monitor plant response dynamics in stress-free conditions⋆

Olivier Pieters, Tom De Swaef, Peter Lootens, Michiel Stock, Isabel Roldán-Ruiz, Francis wyffels

- Study of eco-physiological plant response dynamics in stress-free conditions
- We acquired a hyperspectral dataset with high spatial and temporal resolution
- Leaf temperature and vapour pressure deficit were estimated with NMSE < 0.23
- PAR and air temperature were estimated with NMSE < 0.06
- Lack of clear treatment limited the model performance of some variables

Limitations of snapshot hyperspectral cameras to monitor plant response dynamics in stress-free conditions

Olivier Pieters[a,b,*], Tom De Swaef[b], Peter Lootens[b], Michiel Stock[c], Isabel Roldán-Ruiz[b,d], Francis wyffels[a]

[a] *IDLab-AIRO – Ghent University – imec, Technologiepark-Zwijnaarde 126, 9052 Zwijnaarde, Belgium*
[b] *Plant Sciences Unit, Flanders Research Institute for Agriculture, Fisheries and Food, Caritasstraat 39, 9090 Melle, Belgium*
[c] *KERMIT, Department of Data Analysis and Mathematical Modelling, Ghent University, Coupure links 653, 9000 Ghent, Belgium*
[d] *Department of Plant Biotechnology and Bioinformatics, Ghent University, K.L. Ledeganckstraat 35, 9000 Gent, Belgium*

Abstract

Plants' dynamic eco-physiological responses are vital to their productivity in continuously fluctuating conditions, such as those in agricultural fields. However, it is currently still very difficult to capture these responses at the field scale for phenotyping purposes. Advanced hyperspectral imaging tools are increasingly used in phenotyping, and have been applied to detect changes in plants in response to a specific treatment, phenological state or monitor its growth and development. Phenotyping has to evolve towards capturing dynamic behaviour under more subtle fluctuations in environmental conditions, without the presence of clear treatments or stresses. Therefore, we investigated the potential of hyperspectral imaging to capture dynamic behaviour of plants in stress-free conditions at a temporal resolution of seconds. Two growth chamber experiments were set up, in which strawberry plants and four different background materials, serving as controls, were monitored by a snapshot hyperspectral camera in variable conditions of light, temperature and relative humidity. The sampling period was set to three seconds, triggering image acquisition and gas exchange measurements. Different background materials were used to assess the influence of the environment and the camera in both experiments. To separate the plant and background data, static masks were determined. Two datasets were created, which encompass both experiments. One dataset was constructed after averaging over the entire mask to acquire one value per spectral band. These values were then used to calculate a set of vegetation indices. The other dataset used spatial subsampling to retain spatial information. From both datasets, linear models were constructed using ridge regression, which estimated the measured eco-physiological and environmental data. Leaf temperature and vapour pressure deficit based on leaf temperature are the two main eco-physiological characteristics that could be predicted successfully. Stomatal conductance, photosynthesis and transpiration rate show less promising results. We suspect that limited variation, and low spectral resolution and range are the main causes of the inability of the models to extract meaningful predictions. Furthermore, the models that were only trained on background data also showed good predictive performance. This is probably because the main drivers for good performing eco-physiological variables are temperature and incident light intensity. Environmental characteristics that have good performance are photosynthetically active radiation and air temperature. Current hyperspectral sensing technologies are not yet able to uncover most plant dynamic eco-physiological responses when plants are cultivated in stress-free conditions.

Keywords: Hyperspectral camera, phenotyping, proximal sensing, dynamic, monitoring

1. Introduction

Plants adapt their physiology continuously in response to fluctuations in the environment. This determines their performance, both in natural ecosystems, as well as in crop systems (Schurr et al., 2006; Arsova et al., 2020). An increasing amount of experimental data suggests that proper acclimation of the

*Olivier Pieters received PhD funding by Special Research Fund (B.O.F.) of Ghent University [grant number BOF17/DOC/324]. Michiel Stock is supported by the Research Foundation - Flanders [grant number FWO17/PDO/067]. The computational resources (Stevin Supercomputer Infrastructure) and services used in this work were provided by the VSC (Flemish Supercomputer Centre), funded by Ghent University, FWO and the Flemish Government – department EWI.

*Corresponding author

Email addresses: olivier.pieters@ugent.be (Olivier Pieters), tom.deswaef@ilvo.vlaanderen.be (Tom De Swaef), peter.lootens@ilvo.vlaanderen.be (Peter Lootens), michiel.stock@ugent.be (Michiel Stock), isabel.roldan-ruiz@ilvo.vlaanderen.be (Isabel Roldán-Ruiz), francis.wyffels@ugent.be (Francis wyffels)

URL: olivierpieters.be (Olivier Pieters)

photosynthesis biochemistry to environmental fluctuations is crucial for plant productivity, and potentially more important than high photosynthesis rates under steady-state conditions (Kaiser et al., 2018; Kromdijk et al., 2016; Vialet-Chabrand et al., 2017; Matthews et al., 2018; Townsend et al., 2018). For instance, when focussing on the water relationships in a plant, changes in the environment cause variation in stomatal conductance which in turn determines leaf transpiration, and consequently leaf cooling as well as plant nutrient uptake.

For example, because the response of the photosynthesis biochemistry to fluctuating light conditions is faster than the kinetics of stomatal conductance, these fluctuations also impact the interplay between plant water and carbon relations (Lawson et al., 2012; Lawson and Blatt, 2014). Consequently, a mismatch arises between CO_2 assimilation and water loss (McAusland et al., 2016). Reducing this mismatch, and improving the capacity of crop photosynthesis to respond to fluctuating light environments is, therefore, a promising avenue for breeding more productive crop varieties (Salter et al., 2019; Murchie and Ruban, 2020).

Given the importance of plant physiological responses to environmental fluctuations, it is essential that new field phenotyping technologies specifically focus on capturing such fast-changing dynamics (Murchie et al., 2018). Yet, it remains difficult to capture plant photosynthetic and water status responses to fluctuating conditions in the field. Gas exchange devices based on infrared gas analysers (IRGA) allow continuous measurements of transpiration and CO_2 assimilation and capture detailed dynamics (Kromdijk et al., 2016). However, this approach does not allow for high-throughput measurements and requires expensive devices. Furthermore, these systems monitor individual leaves and do not provide concurrent data at the plant scale, while recent evidence points out that plants display systemic responses under fluctuating light conditions (Shimadzu et al., 2019).

Chlorophyll fluorescence imaging is a powerful method to monitor the photosynthetic capacity of plants (Baker, 2008; Murchie and Lawson, 2013). However, chlorophyll fluorescence measurements typically require a dark adaptation period of one hour, which limits the applicability to study short-term dynamics. New developments in chlorophyll fluorescence imaging methods like Light-Induced Fluorescence Transient (LIFT) or Sun Induced Fluorescence (SIF) overcome this dark adaptation period and can be used as proxies. These methods can be applied at different scales and show great promise, though they do not enable acquisition of absolute photosynthesis biochemistry data, and still require extensive calibration (Murchie and Ruban, 2020; Bandopadhyay et al., 2020).

Moreover, chlorophyll fluorescence imaging is unable to monitor stomatal conductance. Because stomatal conductance is closely related to leaf temperature, thermal sensors can be used to monitor it by applying basic energy balance equations (Jones, 2004; Maes and Steppe, 2012). These equations require the assessment of the micro-environmental conditions of the leaf and the boundary layer resistance to water vapour (Jones et al., 2002). Although most studies with thermal sensors use single time point observations, continuous monitoring of dynamic stomatal conductance in response to a fluctuating environment is possible and can be combined with chlorophyll fluorescence imaging to link plant water relations and photosynthesis (McAusland et al., 2016).

Generally, field phenotyping uses imagery that captures the plants' reflectance in different wavelengths. This information can be used to determine specific plant traits. Examples include, but are not limited to, detection of biotic and abiotic stress, and estimation of nitrogen content and yield. Mir et al. (2019) provides an overview of current methods. In this respect, broadband RGB cameras are often used in phenotyping experiments because they are inexpensive and can be used to monitor plant growth at the scale of days and weeks, or to develop spectral indices referring to the greenness or canopy cover (Borra-Serrano et al., 2020). However, these sensors do not provide information on dynamic responses of photosynthesis over time scales of seconds or minutes.

Hyperspectral imaging sensors capture reflectance in many wavelengths and are increasingly applied in phenotyping research. Hyperspectral imaging has already been applied to various settings that benefit from higher spectral resolutions to detect biotic and abiotic influences on plants (Khan et al., 2018). Examples of studies on biotic factors include blight caused by *Alternaria solani* in potato (Van De Vijver et al., 2020), late blight caused by *Phytophthora infestans* in potato (Franceschini et al., 2019), or tracking the development of three foliar diseases in barley (Wahabzada et al., 2016). Mahlein (2015) and Lowe et al. (2017) provide comprehensive overviews of plant disease detection using imaging sensors and hyperspectral sensors specifically. Studies in which hyperspectral imaging was used to investigate plant responses in interaction with abiotic factors include, for example, detection of green citrus fruits on trees (Okamoto and Lee, 2009), nitrogen deficiency in sorghum (Zhao et al., 2005), seasonal structural changes and a heterogeneous architecture in an olive orchard (Zarco-Tejada et al., 2013b), nitrogen and water distribution quantification in wheat (Bruning et al., 2019), and drought stress in barley and saxaul (Behmann et al., 2014; Jin and Wang, 2016). One common aspect that all the aforementioned studies share, is the presence of a clear treatment or perturbation that results in substantial stress or that influences the phenology of the plant. Furthermore,

they usually monitor plants over extended periods, often months or an entire growing season, typically with several days to a week between measurements.

However, to the best of our knowledge, there is no research yet on hyperspectral data concerning photosynthetic activity at high spatial and temporal resolution in the seconds to minutes range. Nonetheless, vegetation indices (VI) and data derived from hyperspectral cameras might have the potential to monitor subtle dynamics on a detailed scale. For instance, the Photochemical Reflectance Index (PRI) offers potential if it can capture variations in the de-epoxidation of the xanthophyll cycle (Alonso et al., 2017) or the Canopy Chlorophyll Content Index (CCCI) which offers a good measure of canopy nitrogen (Barnes et al., 2000).

We believe that new phenotyping technologies should increasingly focus on capturing dynamics in photosynthesis biochemistry and stomatal conductance kinetics under stress-free yet fluctuating conditions. The objective of the present study is to evaluate the potential of hyperspectral snapshot cameras for this purpose. More specifically, we aim to capture the dynamic responses of strawberry plants in fluctuating, yet stress-free environmental conditions. To this end, experiments were conducted in growth chambers because they offer excellent controllability of the environment over field experiments.

2. Materials and Methods

2.1. Measurement Set-up

The experimental set-up consisted of a single strawberry plant (*Fragaria* × *ananassa*), placed inside a growth chamber of 1.45 × 0.77 × 1.45 m (height × depth × width) (BIOCLIM 1600 US, Weiss Technik, Reiskirchen, Germany). Light intensity, temperature and relative humidity were controlled by a microcontroller board (Dwenguino, Dwengo vzw, Brussels, Belgium), placed outside the growth chamber. The temperature and relative humidity of the growth chamber were controlled using analogue signals, and varied randomly between 11 °C and 33 °C, and 31 % and 75 % respectively.

A custom-built frame of 1.00 × 0.70 × 1.10 m (height × depth × width) was inserted into the chamber. On top of which a grid of lamps was mounted, consisting of 32 LED lamps (MAS LED spot VLE D 4.9-50W GU10 927 60D, Koninklijke Philips N.V., Amsterdam, The Netherlands) and twelve halogen lights (DECOSTAR 51 PRO 50 W 12 V 36° GU5.3, OSRAM GmbH, Munich, Germany). The halogen lights were used as broadband light source, providing illumination in the visible and infrared range, while the LED lights increased the total Photosynthetically Active Radiation (PAR) while keeping thermal radiation within limits. Graphical depictions of the emission spectra are provided in fig. 11. The light intensity of the halogen lamps was controlled using a Digital Addressable Lighting Interface (DALI) controller and bus, while the LED lights were arranged in four sets that could be individually turned on and off. A detailed overview of the grid is depicted in fig. 1.

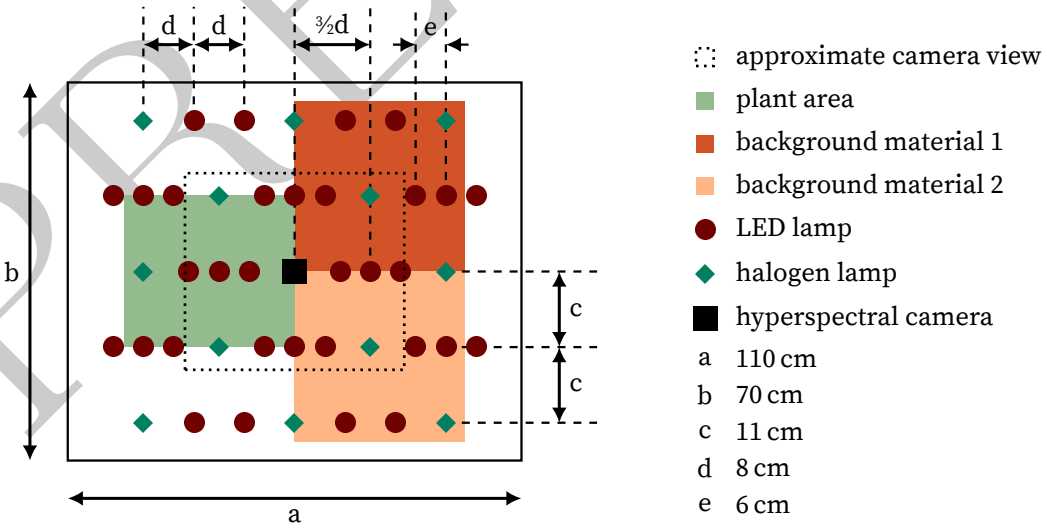

Figure 1: Schematic representation of the light and camera arrangement above the plant and background materials.

A single strawberry leaf was inserted into a transparent leaf chamber of the LI-6400XT photosynthesis system (LI-COR, Lincoln, NE, USA) to acquire gas exchange measurements (transpiration and photosynthesis). The control board also controlled the sampling time steps of the LI-6400XT, using a custom circuit that was connected to the manual sample button on the measurement node. To increase the carbon dioxide

concentration in the growth chamber, a constant influx of stabilised air was used. This influx had a carbon dioxide concentration of 500 ppm at a rate of $1\,m^3\,h^{-1}$. For environment sensing at canopy height, we measured the temperature, light intensity and relative humidity. An external probe (Vaisala 50Y, Vaisala, Helsinki, Finland) was used to measure temperature and humidity. The gas exchange device has a PAR probe to measure light intensity. This device was programmed to recreate the temperature measured using the probe inside the chamber, thus preventing the chamber from heating-up due to infrared radiation.

In the centre of the lamp grid, a hyperspectral camera consisting of two camera heads (EP-12, 3D-One, Sulz, Austria) was placed to monitor the plant. One head is sensitive light in the near-infrared (NIR), while the other is sensitive to the visible range (VIS). We refer to these as H1 and H2, respectively. Both heads capture 12-bit colour information. The sensors were constructed by IMEC (Leuven, Belgium). H1 captures light in 25 spectral bands and has a spatial resolution of 403×216. H2 captures light in 16 spectral bands and has a spatial resolution of 504×270. A trade-off was made here between spectral accuracy and sampling rate. We set the sampling period to 3 s, which was too fast for using a high-resolution line-scanning sensor. The snapshot camera used here can capture images up to 120 Hz. One spectral filter was used for each sensor to limit the sensitivity range of the visible (VIS) or near-infrared (NIR) spectra. The NIR filter was a long pass filter, starting at 675 nm and cuts-off at 1650 nm (TECHSPEC 675nm 25mm Dia, High Performance Longpass Filter, Edmund Optics, Barrington, NJ, USA), while the VIS filter (SCHOTT BG38, Edmund Optics, Barrington, NJ, USA) starts at 350 nm and cuts-off at 645 nm. This camera does not support an external trigger source, thus the internal trigger source was configured to sample every 3 s. When the responses of the cameras were taken into account, this set-up observed wavelengths in the ranges 400 nm to 645 nm, and 675 nm to 1000 nm for H1 and H2 respectively. An illustration of the entire set-up is shown in fig. 2.

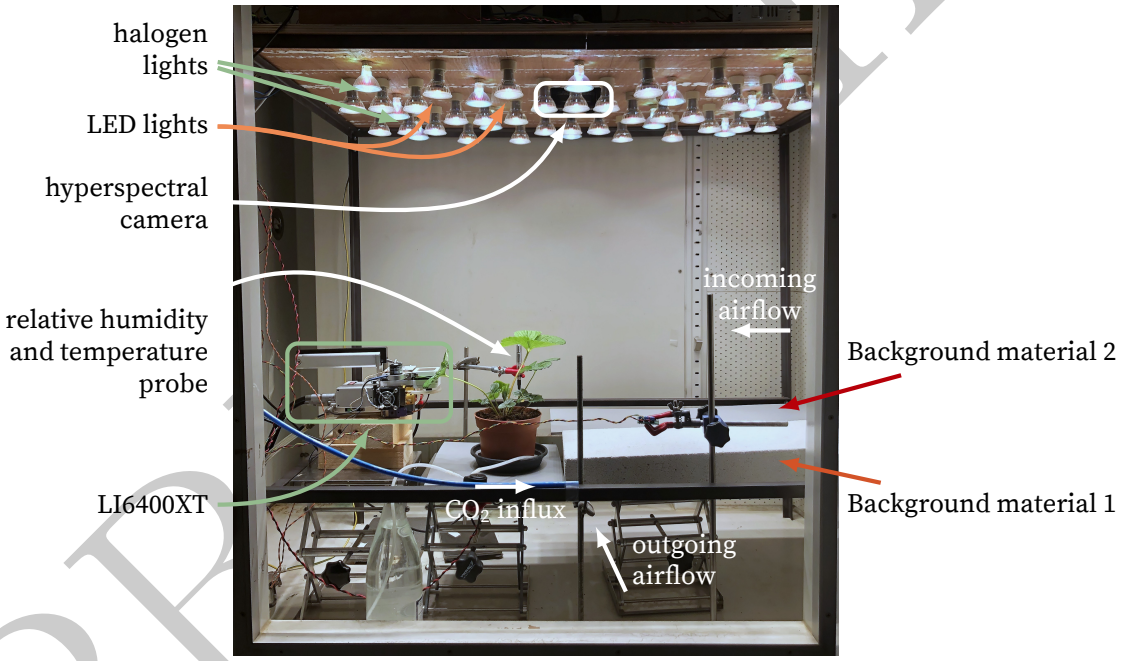

Figure 2: Experimental set-up inside the growth chamber. The plant (strawberry) was raised to increase the area of the leaf in the images. The sensors (photodiodes, relative humidity and temperature sensor) were mounted at canopy height. The hyperspectral camera was mounted directly above the plant. Twelve halogen lights were mounted at the same height as the camera. A grey PVC plate was used to provide a uniform background.

The spectral peak wavelengths for H1 and H2 are depicted in tables 3 and 4. The spectral resolution of H1 varies between 6 nm and 25 nm, while the spectral resolution of H2 varies between 2 nm and 14 nm.

A camera always makes an indirect observation, so there might be unwanted interference with the measurements. For instance, the reflective properties of surrounding materials can change, which interferes with the plant measurements. To investigate this, we also included different background materials in the analysis. Four materials were investigated: plywood (hardwood, Van Den Nest, Aalst, Belgium), non-reflective black cotton cloth (Veritas, Kontich, Belgium), grey polyvinyl chloride (PVC) (Scafoam, Scala, Wetteren, Belgium), and Ytong (Xella, Duisburg, Germany). It was not possible to have similar lighting conditions on all four materials simultaneously. Consequently, the experiment was conducted twice. The first experiment used PVC and plywood, while the second used Ytong and cloth. The second experiment was conducted four days after the first one on a different plant. Both plants were grown in the same greenhouse in close

proximity, and thus experienced similar conditions before the experiment. Each experiment lasted for 100 h. Temperature, relative humidity and light radiation were randomly varied, but the same time series was used in both experiments. To generate these random sequences, samples were drawn from a uniform distribution. These distributions ranged between 8.8 °C to 32.6 °C and 38.8 % to 94.6 % for temperature and relative humidity respectively. These are the set values, which differ from the measured values mentioned above, because the growth chamber was not always able to respond sufficiently fast to the target conditions. The halogen lights were controlled digitally using the DALI interface with brightness vales between 196 (0xC4) and 254 (0xFE) (the maximum value), while the four sets of LED lights were set by sampling a number between 0 and 15, where each bit corresponds to the status of a lamp set.

2.2. Data Preparation and Processing

The set-up consisted of two independent data sources: the gas exchange system and the hyperspectral camera. They were not synchronised due to the lack of a common trigger source. Hence, the start of measurement was not aligned. This difference was manually corrected by turning on all LED lights at the start of the experiment. Furthermore, the camera did not always sample consistently. As a result, the time points of the images did not always align with those of the gas exchange system. Both the gas exchange and hyperspectral camera systems provide a sample timestamp. Synchronisation of both sources was achieved using the time points of both sources and linear interpolation to construct sample points on a single time axis.

Time drift between both was negligible for the duration of the experiment because the sample rate was 3 s and the duration of the experiment was only 100 h. The camera had an internet uplink and was synchronised to a Network Time Protocol (NTP) server. Typical synchronisation offset with NTP-servers are lower than 10 ms (Marouani and Dagenais, 2008). The LI6400XT has an accurate internal clock that has at most 0.5 s drift after 92 days (Li-Cor Inc., 2012). Consequently, it is safe to ignore the drift between the two systems.

Photosynthesis is driven to a large extent by light. To maximise the variation in photosynthetic activity of the plant, a substantial range in illumination intensity was applied. Because a camera requires light to operate, the light was never fully turned off. The lowest PAR value that was applied was 70 µmol m^{-2} s^{-1}, while the highest was 409 µmol m^{-2} s^{-1}. The camera was set to automatic exposure optimise the dynamic range of each image and reduce over- and underexposed areas. In low illumination conditions, there was a considerable amount of noise. Consequently, after aligning and resampling of the data, the data was further processed using a uniform blur filter of 5×5 pixels, to reduce noise in the image. Additionally, the data was rescaled and converted to floating-point to compensate for the variable exposure duration. Details of this transformation are included in the appendix (section 8.2).

The leaves of the strawberry plant displayed limited motion from reorientation, as is evident from fig. 3. Hence, no motion compensation was applied to the image sequence to reduce computational complexity. This also simplified the masking that had to be applied to separate the plant from the background. Each data type has its own mask, which was manually determined and validated. To this end, all images were averaged and a the relevant pixels were selected manually. The validation was performed by generating a video sequence with the mask on top. There are also different masks for the VIS and NIR cameras since they observe the experiment from a different location. Thus, each of the six data types has two masks, one for each camera, resulting in a total of 12 masks.

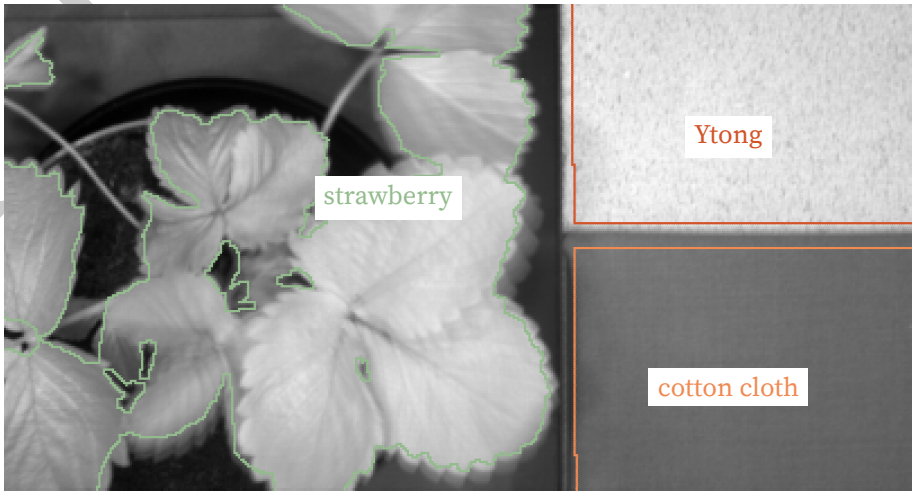

Figure 3: Averaged image from every 10th image from the start to the end of the experiment of H1 in the second experiment.

Image data are highly correlated, especially for adjacent pixels. Therefore, we constructed two types of datasets. The first dataset averaged over all spatial locations of each mask, to obtain a new data entry. This technique drastically reduced the number of features at each sample point from over 10,000[1] to 41. 25 from the NIR camera (H1) and 16 from the VIS camera (H2). We use the following shorthand notation *(25+16)* to denote the number of samples per camera (NIR+VIS). To incorporate spatial effects, a second dataset was constructed using subsampling. The images were spatially sampled randomly without duplicates. When a certain location was considered, all spectral bands were included in the dataset. Subsampling sizes varied between 3 (1+2) and 200 (78+122) for both experiments. The split was designed to have a similar number of features of H1 and H2 at each sample point. Subsampling and averaging also helped to deal with the large amount of data that was captured during the trial. Each image from either H1 or H2 had a size of 4.3 MB, and there were approximately 130,000 valid data points per trial, resulting in a total dataset size for both trials of slightly more than 2 TB.

VIs are often used to extract meaningful information from image data, also in hyperspectral imaging (Vogelmann et al., 1993; Rouse et al., 1974; Gitelson and Merzlyak, 1994; Sims and Gamon, 2002; Gamon et al., 1992; Behmann et al., 2014; Jin and Wang, 2016; Gao et al., 2018; Alonso et al., 2017). However, only a limited and non-uniformly spaced number of bands are available here, limiting the possibilities to use VIs from literature. Therefore, we generated a custom set of VIs. Based on literature, and taking practical limitations of the number of variables into account, we limited the created VIs to combinations of fractions of band pairs, summarised by eqs. (1) and (2). All possible combinations of two spectral bands were generated. Equation (1) is the fraction (F), and eq. (2) is the normalised fraction (NF) of a pair of bands. The model automatically selected the relevant indices thanks to regularisation (see below). The spectral bands from H1 were numbered 0 through 24, and those of H2 25 to 40. An index was only included if the absolute value of the maximum value of all Pearson correlation coefficients (ρ) with already included indices was lower than 0.95. This boundary ensures that none of the features were (nearly) linearly dependent. Note that the included VIs need not be the same for the different data types since the correlation metric might differ. This technique could generate up to 2459 new features.

$$VI_{ij}^{F} = \frac{C_i}{C_j}, \qquad i \in \{0, 1, \ldots, 40\}, j \in \{0, 1, \ldots, i-1, i+1, \ldots, 40\} \tag{1}$$

$$VI_{ij}^{NF} = \frac{C_i - C_j}{C_i + C_j}, \quad i \in \{0, 1, \ldots, 39\}, j \in \{i+1, i+2, \ldots, 40\} \tag{2}$$

Normally, VIs are only generated on image data from plants, but we also generated them for the background materials to avoid bias due to the generation of possibly more informative features in the comparison between plant- and background-based models.

To assess the variability in performance due to the subsampling in the second dataset, nine independent subsets were constructed of each subsample size. Consequently, partial overlap between datasets was possible.

A linear model combined with Tikhonov (or L2) regularisation (Tikhonov, 1963), commonly called ridge regression, was used to fit the camera data to the environmental and eco-physiological data. Such a model is well-suited to demonstrate correlations between different datasets and should provide improved prediction performance compared to only using indices (Yendrek et al., 2017). It is guaranteed to provide the global optimum and is very fast to fit. This is important since hyperspectral cameras generate vast amounts of data. The Tikhonov regularisation prevents the model to overfit by including the model weights into the optimisation target. The whole pipeline was implemented in Python, with the help of the Pandas (McKinney, 2010, 2011) and Scikit-Learn (Pedregosa et al., 2011) libraries and has been open-sourced on GitHub[2]. Part of the dataset is also available with an open-access licence on Zenodo (Pieters et al., 2020).

Ridge regression has one hyperparameter that must be optimised. This parameter determines the total magnitude of the model coefficients. As a result, each time series had to be split into three categories: training, validation and test data. The training data was used to train the coefficients of the model, while the validation data was used to select the optimal hyperparameter. The test data was employed to evaluate the performance on unseen data. This latter type of data was not used to optimise the model in any way and thus provided a good indication for the actual performance of the model. To eliminate possible day-night rhythms, the data was split into batches of 3000 samples (2.5 h), while 1500 samples (1.25 h) between batches were discarded to eliminate the correlation between adjacent batches. This decorrelation was verified after

[1]The number of features is dependent upon the type of data (plant1, plant2, cotton, Ytong, PVC or wood) and the experiment.

[2]`https://github.com/opieters/hyperspectral-analysis`

the analysis through an offset between the target and input data (not shown). After selecting the optimal hyperparameter, a final model was trained on both the train and validation data. This ensures optimal data use.

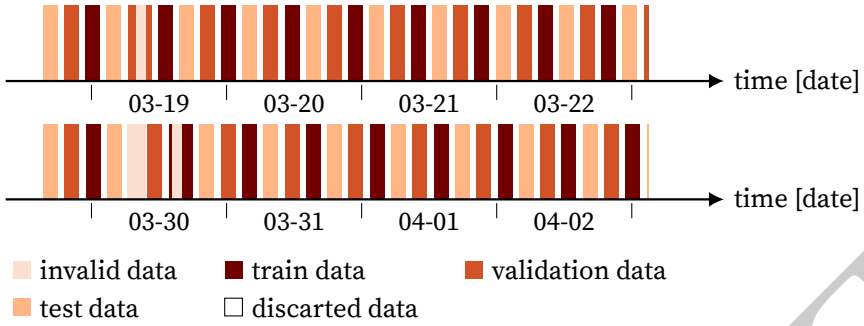

Figure 4: Visualisation of the data split in training, validation, and test data for both experiments.

In summary, three different types of linear models were generated based on six different data types. The three model types refer to the kind of input features presented to the model. In the first case, the model was trained on the averaged spectral bands. In the second case, VIs were added to the input feature set. This data-augmentation enabled the model to leverage non-linear dependencies in the data. In the third and final case, the input features consisted entirely of spectral bands, but without averaging over the entire mask. Different materials give rise to distinct data types; plant1, plant2, wood, PVC, Ytong and cotton were the materials considered in this study.

2.3. Error Metric

To estimate the modelling capacity of the camera system, different models were created that estimate environmental and eco-physiological data. Comparing the performance of different tasks is crucial. To that end, the normalised mean squared error (NMSE) metric was used:

$$\mathrm{NMSE} = \frac{\frac{1}{N}\sum_{t=0}^{N-1}(y(t) - \hat{y}(t))^2}{\mathrm{var}(y)} \tag{3}$$

where $\hat{y}(t)$ is the predicted value from the model, $y(t)$ is the actual value, $\mathrm{var}(\cdot)$ computes the variance and N is the total number of samples considered. This metric has several advantages over a traditional mean squared error comparison. In the first place, it takes the variability of the target signal into account. This eliminates a possible bias towards slow varying signals. Additionally, interpretability is very straightforward. An NMSE of 1.0 corresponds to the mean prediction for all samples, since the numerator reduces to the variance, while an NSME of 0.0 corresponds to a perfect prediction. This property makes it very easy to compare and interpret NMSE values.

2.4. Variables and Eco-physiological Meaning

The gas exchange measurement device (LI6400XT) produced the eco-physiological data to which the hyperspectral image data was fitted. Different environmental and eco-physiological parameters were captured, providing a diverse set of target variables. An overview of the available variables is provided in table 1. All variables except for air temperature (T_{air}) and relative humidity (RH) were measured outside the area observed with the camera. This was a requirement due to the high reflectivity of the leaf chamber that resulted in an undesired exposure compensation of the camera.

3. Results

The data were analysed in three steps: first, the environmental conditions were investigated to better understand the eco-physiological responses of the plant in the second and third step. The averaged dataset was augmented with VIs and analysed in the second step, and the subsampled dataset was studied in the third and final step.

Table 1: Overview of considered environmental and eco-physiological variables.

abbreviation	description	unit	sensor
P_n	photosynthetic rate	$\mu\mathrm{mol}(CO_2)\,\mathrm{m}^{-2}\,\mathrm{s}^{-1}$	LI6400XT
g_s	stomatal conductance	$\mathrm{mol}(H_2O)\,\mathrm{m}^{-2}\,\mathrm{s}^{-1}$	LI6400XT
Tr	transpiration rate	$\mathrm{mmol}(H_2O)\,\mathrm{m}^{-2}\,\mathrm{s}^{-1}$	LI6400XT
VPD_leaf	vapour pressure deficit based on leaf temperature	kPa	LI6400XT
T_leaf	leaf temperature	°C	LI6400XT
T_air	air temperature (growth chamber)	°C	Vaisala 50Y
RH	relative humidity (growth chamber)	%	Vaisala 50Y
PAR	photosynthetically active radiation (growth chamber)	$\mu\mathrm{mol}\,\mathrm{m}^{-2}\,\mathrm{s}^{-1}$	LI6400XT

3.1. Analysis of the Environmental Conditions

Normalised density plots of the environmental conditions are depicted in fig. 5. These indicate that PAR vs. RH ($\rho = -0.05$) and PAR vs. T_air ($\rho = -0.04$) did not show bias towards particular values of either parameter. This is, however, not the case for RH vs. T_air ($\rho = -0.27$), due to the inability of the growth chamber to settle at the target point before a new one was set. A combination of low T_air and low RH was not achieved (see fig. 5 (c), lower left corner). High RH values are also less prominent than low ones.

Similar observations were made for the second experiment (not depicted) since the random target sequence was the same for both experiments to simplify the comparison between both extracted datasets. As expected, the main environmental conditions in the growth chamber covered a wide range, but extreme values that cause strong stress conditions were avoided.

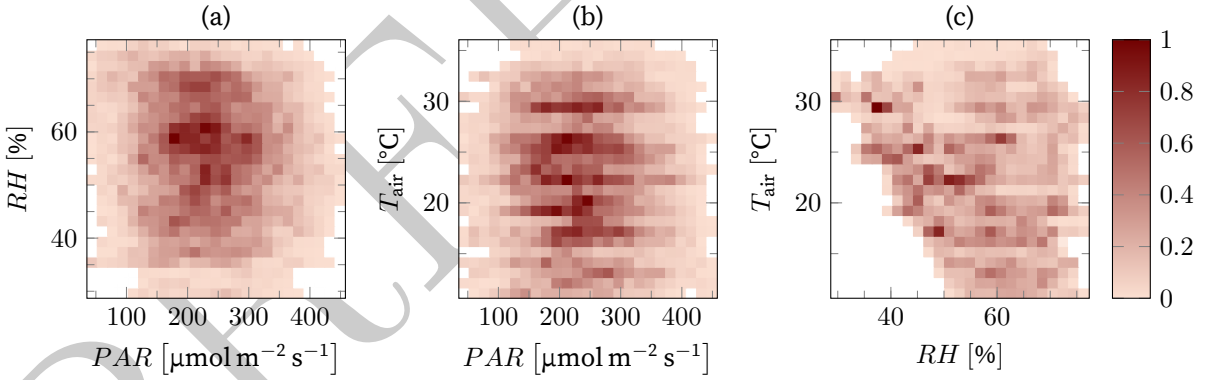

Figure 5: Normalised density plots of the most important environmental conditions: PAR, air temperature (T_air) and relative humidity (RH) in the growth chamber for the first experiment. The second experiment had similar densities.

3.2. Analysis of the Averaged Dataset

First, we analysed the smaller dataset. This is the dataset that was constructed after averaging over the entire mask, resulting in a single value per spectral band and per mask type. VIs were also generated from the spectral bands. These features were then fitted to target eco-physiological and environmental variables. An overview of the model performance for each data type is depicted in fig. 6. Models with VIs are shown using coloured bars, while models without VIs are depicted using a bar with only a blue border. Numeric values are also included in table 5.

The performance for most photosynthetic rate (P_n), stomatal conductance (g_s) and transpiration rate (Tr) is poor, both with and without VIs. Better performance is observed for T_leaf and to a lesser extent VPD_leaf. The entire time series of VPD_leaf for plant2 is depicted in fig. 7 for visual inspection. There are several regions where the data fitted very well, but in other parts, there was significant offset from the measured variable, especially at the extremes. Though the model usually follows the correct trend.

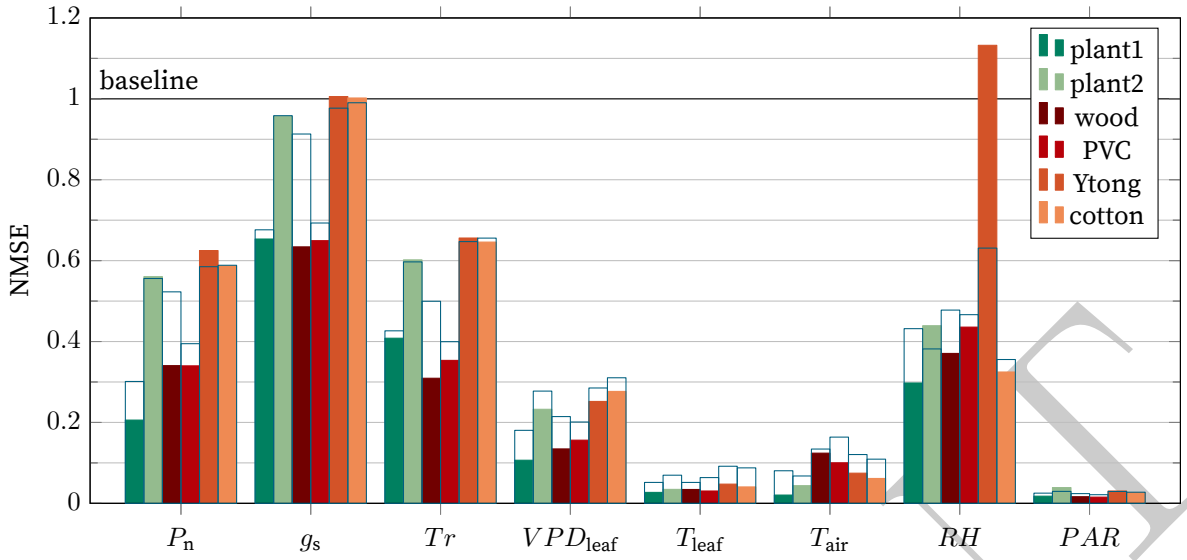

Figure 6: Performance of the linear model for different eco-physiological and environmental parameters. The lower the NMSE, the better. The coloured bars represent models that were trained with raw image data and vegetation indices (VI), while the blue bordered bars are those without VIs.

Visualisations of different tasks for the plant2 time series are depicted in fig. 8. From this figure, it is clear that models with a high NMSE value have very low extraction efficiency. We consider a fit sufficient if the NMSE value is equal to or below 0.25 for both plant models.

While NMSE provides an objective comparison, correctly followed trends such as in the case of P_n in fig. 8 are not reflected in a low NMSE score. This is due to a continued offset between the correctly predicted trends and the measured variable. The prediction of Tr has a better NMSE score because the predicted values approximate an averaged version of the measured variable.

Eco-physiological tasks with high NMSE values also display major differences in modelling performance between batches of test data (not visualised). This further indicates that the model was unable to extract meaningful information from the spectral features and VIs. The information was either masked by interferers or the camera was unable to capture changes related to these variables.

For most tasks, there was limited improvement or even reduced performance by adding VIs. Improved performance is strongest for VPD_{leaf}, T_{leaf}, and T_{air}. Reduced performance on the test data can be attributed to overfitting of the model. The performance on the training set has improved, but the models' ability to generalise has decreased, leading to reduced performance. This is especially visible in the case of RH when using Ytong-data. The NMSE value rises from 0.63 to 1.13, above the baseline.

For all physiological variables, plant1 and plant2 are expected to have better performance than the background materials. However, this is not the case for plant2. While the differences between the plant2 and the background present in the same trial (Ytong and cotton) are low, there is a large difference between plant1 and plant2 for both the average modelling performance of P_n, g_s and Tr.

From the environmental variables, T_{air} and PAR has the highest extraction precision. RH has a similar NMSE score for all data types except for Ytong.

	$VPD_{\mathbf{leaf}}$	$T_{\mathbf{leaf}}$	$T_{\mathbf{air}}$
$VPD_{\mathbf{leaf}}$	1.0	0.89	0.76
$T_{\mathbf{leaf}}$	0.89	1.0	0.92
$T_{\mathbf{air}}$	0.76	0.92	1.0

Table 2: Pearson correlation coefficients (ρ) of the two well-performing physiological tasks, leaf temperature (T_{leaf}) and vapour-pressure deficit (VPD_{leaf}), and air temperature (T_{air}).

3.3. Analysis of the Subsampling Dataset

The averaged dataset loses the differences in response due to for instance the age of a leaf. Including such dynamics can yield improved performance. This subsampled dataset investigates this by including randomly

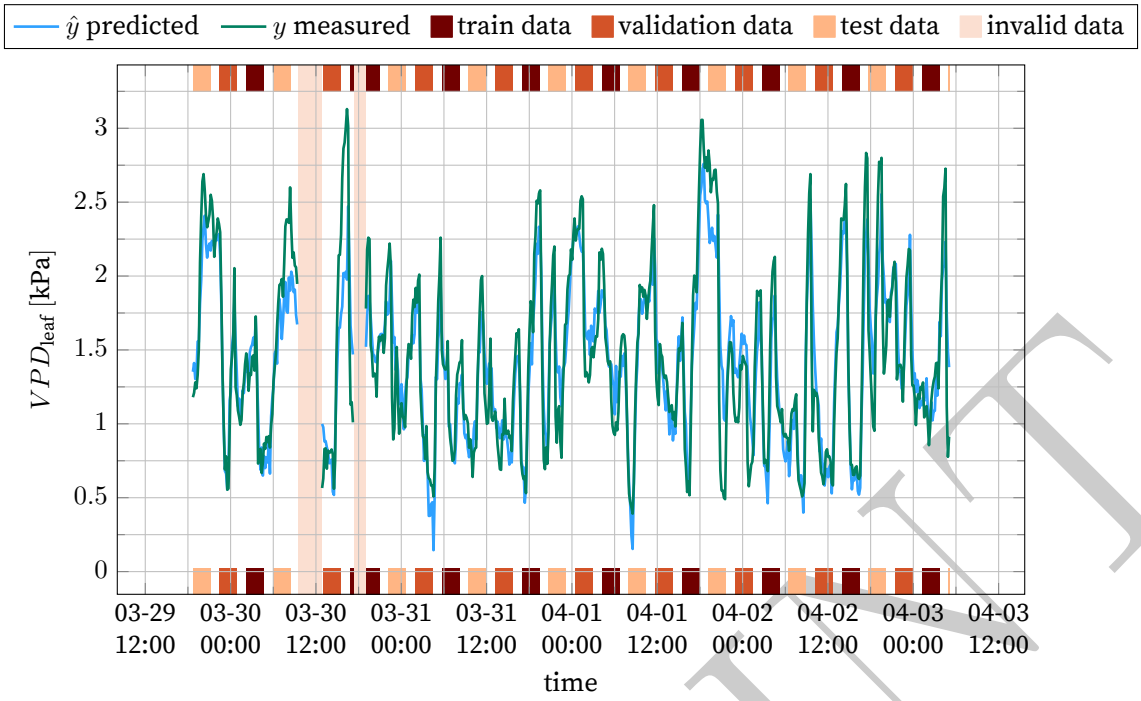

Figure 7: Visualisation of the vapour pressure deficit (VPD_{leaf}) of plant2 data y and the model prediction $\hat{y}$. The model was trained from the first dataset with vegetation indexes. The different data split types are also indicated. The NMSE values for the train, validation and test data are 0.132, 0.273, and 0.233 respectively.

sampled pixels. The ridge model is able to automatically differentiate between more and less relevant pixels, because of the regularisation. The analysis itself was similar to that of the previous section.

Figure 9 displays the performance for the same set of tasks as fig. 6. Error bars are depicted in black. They were computed from the difference in NMSE value arising from the subsampling. The performance of the tasks is similar to that of the previous dataset without VIs. These are not included here because it would drastically grow the number of features, which is undesirable. Table 6 provides the same information as fig. 9 in numeric form.

The number of samples is an important metric for this dataset. Figure 10 visualises the effect of the number of features to the modelling accuracy for T_{air} and Tr. The standard deviation is depicted as a shaded area around the curve in the same colour. As expected, the NMSE decreases with an increasing number of features. The largest subsample size generally offers the best performance, but for underperforming tasks such as Tr, the variance between different batches tends to increase with an increasing number of samples, especially for plant-data. This further illustrates the lack of useful information in the dataset for this particular task.

4. Discussion

The only eco-physiological variables with good performance for both plant time series are VPD_{leaf} and T_{leaf}. However, the background is also good at predicting these. This can be explained by the high correlation between T_{air} and the variables VPD_{leaf} and T_{leaf}, depicted in table 2. VPD_{leaf} is driven by relative humidity and leaf temperature, which are in turn affected by air temperature, light intensity and water status (Amitrano et al., 2019). The reflection spectrum of plants in the near-infrared region varies when the air temperature changes (Carter et al., 2000). These changes are probably detected by the model, leading to good performance of temperature-related variables. The backgrounds considered here might have similar reflective properties. Though their structure cannot change as in the case of plants, they can radiate more or less infrared light, enabling the model to extract the temperature (Beltrán et al., 1997). The spectrum at two different temperatures is depicted in fig. 12. The spectra of both materials and the plant have changed in the near-infrared region.

The results for g_{s} are in line with previous research by Zarco-Tejada et al. (2013a), who used a similar wavelength range from 400 nm to 900 nm and were also unable to extract this parameter. However, others have reported successful extraction of g_{s}. Rapaport et al. (2015) were able to assess g_{s} in grapevine, chiefly using the WABI-3 VI. This index uses a spectral band at 1485 nm, which indicates that a wider spectral

range is necessary to assess g_s. Moreover, Rapaport et al. (2015) induced a clear treatment. Grapevine leaves were subjected to water-stress, causing stronger changes in g_s.

The possibility to estimate P_n from hyperspectral data in maize has been reported by Yendrek et al. (2017). They were able to predict the CO_2-saturated rate of photosynthesis (V_{max}) from hyperspectral imaging and a partial least squares (PLS) regression model. They indicated important peak wavelengths at 554 nm and 719 nm. Though the VIS and NIR cameras have nearby bands at 552 nm and 724 nm, there are fewer bands available compared to the study by Yendrek et al. (2017), which acquired the spectral reflection of maize at a resolution of 1 nm. While their results are significant for V_{max}, the results are probably insufficient to capture the subtle dynamics of the study presented in this paper. Due to the two treatments that were applied in the study by Yendrek et al. (2017), low nitrogen availability and elevated ozone concentrations, V_{max} varied from approximately 7 µmol m^{-2} s^{-1} to 62 µmol m^{-2} s^{-1}, while P_n only varies from 3.1 µmol m^{-2} s^{-1} to 14.7 µmol m^{-2} s^{-1}. Furthermore, their model also has a root mean square error (RMSE) score of 6.6, resulting in low predictive performance for the range of the current study, and thus also has limited applicability to monitor small changes of P_n.

As mentioned in the introduction, SIF is a promising indicator of photosynthetic activity. It originates from initial reactions in Photosystem II and I, which have narrow peaks around 690 nm and 760 nm respectively. Resolving these peaks requires high spectral resolution ($\leq$ 5 nm), which is not possible with the technology used in this study (Bandopadhyay et al., 2020). A snapshot camera with improved resolution should be able to compute SIF and thus be able to better assess photosynthetic activity.

Unlike the current study, Weksler et al. (2020) were able to measure Tr with hyperspectral imagery in young pepper plants. They used a selection of spectral bands at 523 nm, 697 nm and 818 nm with high spectral resolution using as VIS-NIR camera (400 nm to 1000 nm). Unlike most studies, the study by Weksler et al. (2020) also characterised momentary transpiration. The major difference between the method from their study to the current one, is the plant age. In this study, mature plants were used, unlike the rapidly growing plants in their experiment. Moreover, they measured transpiration using a balance, not with a gas exchange system.

From these studies, we identified four causes that might explain the poor results for g_s, P_n, and Tr. First, the spectral range was insufficient. More specifically, higher wavelengths up to at least 1500 nm are needed to assess these properties based on literature. Second, the spectral resolution needs to increase to preferably 1 nm, and the band spacing should be more uniform. Third, other studies which investigated eco-physiological properties applied clear treatments (Zhao et al., 2005; Zarco-Tejada et al., 2013b; Behmann et al., 2014; Silva-Perez et al., 2018). These cause more pronounced spectral and eco-physiological changes. Therefore, estimation is more direct and less prone to disturbances that mask eco-physiological changes. Fourth, the plant species and age also have an effect on the plant dynamics, where young plants are expected to have stronger variation.

Additionally, a camera is a sensor *at a distance*, meaning that there is no direct contact with the imaged object. This has both positive and negative consequences. The main positive effect is limited to no interference with the object and rapid capture of large amounts of data. However, this creates a disadvantage also due to the distance between object and sensor. There might be interfering materials present that can distort the measurement. For instance, the transmittance of the air layer between the camera and the sample can change depending on environmental changes. Similarly, the reflective properties of materials present in the growth chamber can also change as a result of variable environmental conditions. These changes are also picked up by the camera and can distort the measurement. Usually, such changes are negligible, but when very subtle variability in the plant is under investigation, they might become important. Moreover, it is difficult to compensate for these possible effects during the analysis.

Both PAR and T_{air} are well assessed for plants and all backgrounds. The good performance of PAR is expected since the camera directly observes light and can reconstruct the spectrum used in the measurement of PAR. As mentioned before, spectral changes due to temperature can explain the good modelling performance of T_{air}. It was verified that the camera's responses are not significantly temperature-dependent other than increased white noise at elevated temperatures (data not presented).

The poor NMSE value of RH from the data is in stark contrast to the other environmental variables. A possible reason why these have a high NMSE value is, that there is no infrared radiation around 2 µm captured by the camera nor emitted by the lights. Consequently, none of the strong absorption peaks of water was captured.

The inclusion of VIs does not improve the results much. Consequently, it is not relevant to investigate each of these indices separately and relate them to physiological processes occurring in the plant. If there would have been a significant improvement by including these empirically created indices, additional analysis and experiments would be needed to identify which indices are the most explanatory and explain why these were found. For instance, the generalisation from one plant to another should be tested by using at least

three plants: one for training, one for validation and one for testing.

5. Conclusion

The experimental study presented in this manuscript investigated the accessibility of gas exchange variables of plants from hyperspectral image data. The novelty of this study is that these parameters were investigated without the presence of strong biotic or abiotic stress factors with high temporal resolution (3 s) over the duration of one week. This setup is relevant to monitor the dynamics of plants' physiological responses. Increasingly, researchers are investigating the dynamic behaviour of plants as these are crucial in determining plant productivity in continuously fluctuating environments such as those in agricultural fields.

The analysis indicated that the information content of the hyperspectral data is low for P_n, g_s, and Tr. A possible explanation is the limited variability due to the much lower treatment effect and low-resolution spectral sensing capabilities. The lack of a clear stress-inducing treatment causes less variation of the eco-physiological variables observed. Induced variations were possibly not significant enough to be detectable among other interfering and noise signals that are present in the image data. Additionally, the spectral resolution and range were limited. Plant species and age can also have an effect on performance. VPD_leaf and T_leaf are good performing eco-physiological tasks. Environmental variables also show varying results. As expected, PAR is well assessed, as is T_air. RH cannot be extracted due to the lack of wavelengths above 2 µm. We suspect that the reflection spectrum changes depending on temperature, which enables the model to accurately predict T_air. T_leaf and VPD_leaf are strongly correlated to T_air might explain why these eco-physiological parameters could be assessed.

Current snapshot hyperspectral technologies are not yet well suited to monitor the dynamic responses of plants. Major improvements upon sensitivity and spectral resolution are probably required to enable the detection of subtle changes of eco-physiological parameters in stress-free conditions.

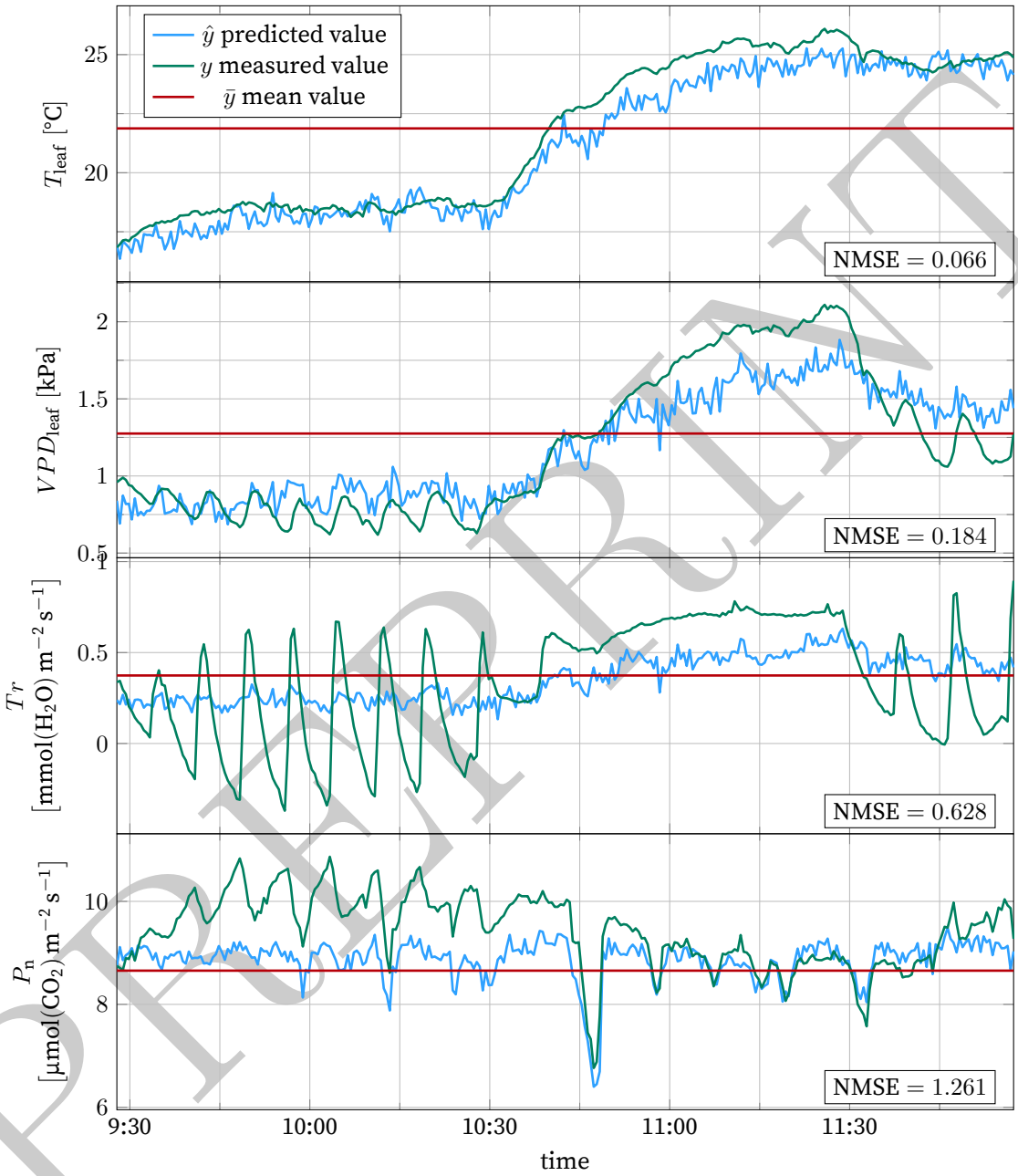

Figure 8: Time plots of the third batch of test data for plant2 for leaf temperature (T_{leaf}), vapour pressure deficit (VPD_{leaf}), transpiration rate (Tr), and photosynthetic rate (P_{n}). The depicted NMSE was computed using the global normalisation factor to prevent possible bias due to batch choice. We can clearly observe a decay in modelling performance as the NMSE increases. y is the measured data, $\hat{y}$ is the model prediction, and $\bar{y}$ is the mean value.

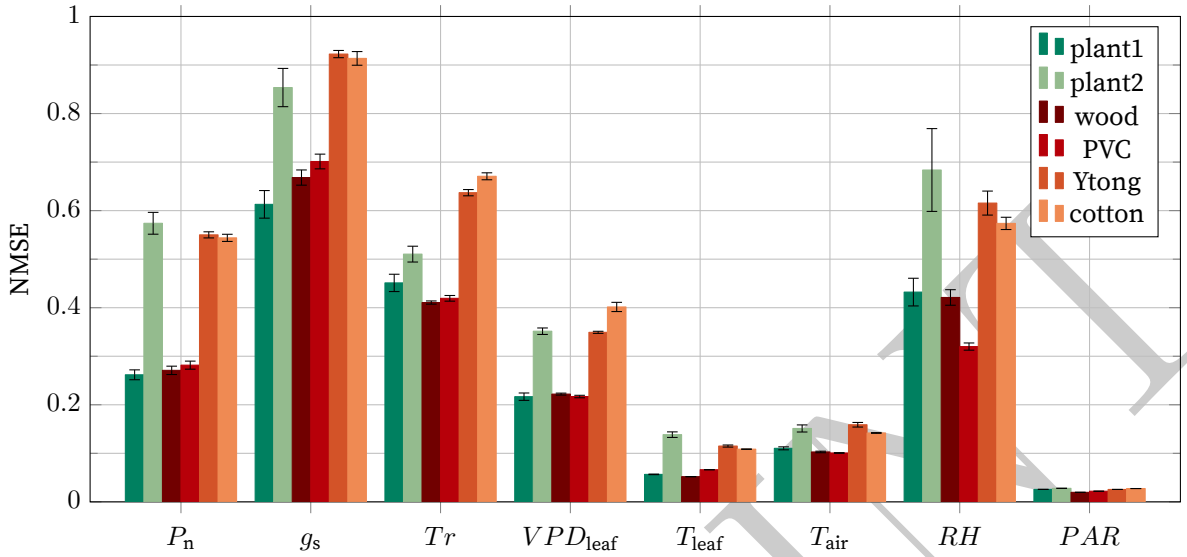

Figure 9: Overview of performance for all variables for a subsample size of 77 (30+47), resulting in 1502 input features for the model.

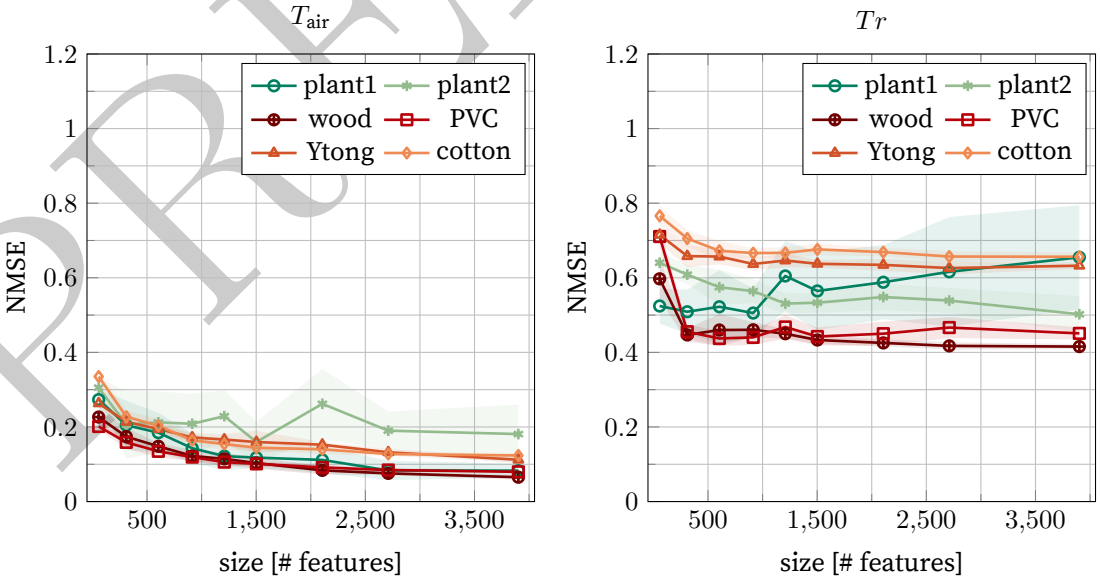

Figure 10: Subsample size effect for the air temperature (T_{air}) and transpiration rate (Tr) tasks.

References

Alonso, L., Van Wittenberghe, S., Amorós-López, J., Vila-Francés, J., Gómez-Chova, L., Moreno, J., 2017. Diurnal cycle relationships between passive fluorescence, PRI and NPQ of vegetation in a controlled stress experiment. Remote Sensing 9, 770. doi:10.3390/rs9080770.

Amitrano, C., Arena, C., Rouphael, Y., Pascale, S.D., Micco, V.D., 2019. Vapour pressure deficit: The hidden driver behind plant morphofunctional traits in controlled environments. Annals of Applied Biology 175, 313–325. doi:10.1111/aab.12544.

Arsova, B., Foster, K.J., Shelden, M.C., Bramley, H., Watt, M., 2020. Dynamics in plant roots and shoots minimize stress, save energy and maintain water and nutrient uptake. New Phytologist 225, 1111–1119. doi:10.1111/nph.15955.

Baker, N.R., 2008. Chlorophyll fluorescence: A probe of photosynthesis in vivo. Annual Review of Plant Biology 59, 89–113. doi:10.1146/annurev.arplant.59.032607.092759.

Bandopadhyay, S., Rastogi, A., Juszczak, R., 2020. Review of top-of-canopy sun-induced fluorescence (SIF) studies from ground, UAV, airborne to spaceborne observations. Sensors 20, 1144. doi:10.3390/s20041144.

Barnes, E.M., Clarke, T.R., Richards, S.E., Colaizzi, P.D., Haberland, J., Kostrzewski, M., Waller, P., Choi, C., Riley, E., Thompson, T., Lascano, R.J., Li, H., Moran, M.S., 2000. Coincident detection of crop water stress, nitrogen status and canopy density using ground based multispectral data, in: Proceedings of the Fifth International Conference on Precision Agriculture, Bloomington, MN, USA.

Behmann, J., Steinrücken, J., Plümer, L., 2014. Detection of early plant stress responses in hyperspectral images. ISPRS Journal of Photogrammetry and Remote Sensing 93, 98–111. doi:10.1016/j.isprsjprs.2014.03.016.

Beltrán, M., García, J.C., Marcilla, A., 1997. Infrared spectral changes in PVC and plasticized PVC during gelation and fusion. European Polymer Journal 33, 453–462. doi:10.1016/S0014-3057(96)00213-3.

Borra-Serrano, I., De Swaef, T., Quataert, P., Aper, J., Saleem, A., Saeys, W., Somers, B., Roldán-Ruiz, I., Lootens, P., 2020. Closing the phenotyping gap: High resolution UAV time series for soybean growth analysis provides objective data from field trials. Remote Sensing 12, 1644. doi:10.3390/rs12101644.

Bruning, B., Liu, H., Brien, C., Berger, B., Lewis, M., Garnett, T., 2019. The development of hyperspectral distribution maps to predict the content and distribution of nitrogen and water in wheat (*Triticum aestivum*). Frontiers in Plant Science 10. doi:10.3389/fpls.2019.01380.

Carter, G.A., Bahadur, R., Norby, R.J., 2000. Effects of elevated atmospheric CO_2 and temperature on leaf optical properties in *Acer Saccharum*. Environmental and Experimental Botany 43, 267–273. doi:10.1016/S0098-8472(00)00048-4.

Franceschini, M.H.D., Bartholomeus, H., van Apeldoorn, D.F., Suomalainen, J., Kooistra, L., 2019. Feasibility of unmanned aerial vehicle optical imagery for early detection and severity assessment of late blight in potato. Remote Sensing 11, 224. doi:10.3390/rs11030224.

Gamon, J.A., Peñuelas, J., Field, C.B., 1992. A narrow-waveband spectral index that tracks diurnal changes in photosynthetic efficiency. Remote Sensing of Environment 41, 35–44. doi:10.1016/0034-4257(92)90059-S.

Gao, J., Nuyttens, D., Lootens, P., He, Y., Pieters, J.G., 2018. Recognising weeds in a maize crop using a random forest machine-learning algorithm and near-infrared snapshot mosaic hyperspectral imagery. Biosystems Engineering 170, 39–50. doi:10.1016/j.biosystemseng.2018.03.006.

Gitelson, A., Merzlyak, M.N., 1994. Spectral reflectance changes associated with autumn senescence of *Aesculus hippocastanum* L. and *Acer platanoides* L. leaves. Spectral features and relation to chlorophyll estimation. Journal of Plant Physiology 143, 286–292. doi:10.1016/S0176-1617(11)81633-0.

Jin, J., Wang, Q., 2016. Hyperspectral indices based on first derivative spectra closely trace canopy transpiration in a desert plant. Ecological Informatics 35, 1–8. doi:10.1016/j.ecoinf.2016.06.004.

Jones, H.G., 2004. Irrigation scheduling: Advantages and pitfalls of plant-based methods. Journal of Experimental Botany 55, 2427–2436. doi:10.1093/jxb/erh213.

Jones, H.G., Stoll, M., Santos, T., de Sousa, C., Chaves, M.M., Grant, O.M., 2002. Use of infrared thermography for monitoring stomatal closure in the field: Application to grapevine. Journal of Experimental Botany 53, 2249–2260. doi:10.1093/jxb/erf083.

Kaiser, E., Morales, A., Harbinson, J., 2018. Fluctuating light takes crop photosynthesis on a rollercoaster ride. Plant Physiology 176, 977–989. doi:10.1104/pp.17.01250.

Khan, M.J., Khan, H.S., Yousaf, A., Khurshid, K., Abbas, A., 2018. Modern trends in hyperspectral image analysis: A review. IEEE Access 6, 14118–14129. doi:10.1109/ACCESS.2018.2812999.

Kromdijk, J., Głowacka, K., Leonelli, L., Gabilly, S.T., Iwai, M., Niyogi, K.K., Long, S.P., 2016. Improving photosynthesis and crop productivity by accelerating recovery from photoprotection. Science 354, 857–861. doi:10.1126/science.aai8878.

Lawson, T., Blatt, M.R., 2014. Stomatal size, speed, and responsiveness impact on photosynthesis and water use efficiency. Plant Physiology 164, 1556–1570. doi:10.1104/pp.114.237107.

Lawson, T., Kramer, D.M., Raines, C.A., 2012. Improving yield by exploiting mechanisms underlying natural variation of photosynthesis. Current Opinion in Biotechnology 23, 215–220. doi:10.1016/j.copbio.2011.12.012.

Li-Cor Inc., 2012. Using the LI-6400 portable photosynthesis system.

Lowe, A., Harrison, N., French, A.P., 2017. Hyperspectral image analysis techniques for the detection and classification of the early onset of plant disease and stress. Plant Methods 13, 80. doi:10.1186/s13007-017-0233-z.

Maes, W.H., Steppe, K., 2012. Estimating evapotranspiration and drought stress with ground-based thermal remote sensing in agriculture: A review. Journal of Experimental Botany 63, 4671–4712. doi:10.1093/jxb/ers165.

Mahlein, A.K., 2015. Plant disease detection by imaging sensors – parallels and specific demands for precision agriculture and plant phenotyping. Plant Disease 100, 241–251. doi:10.1094/PDIS-03-15-0340-FE.

Marouani, H., Dagenais, M.R., 2008. Internal clock drift estimation in computer clusters. Journal of Computer Systems, Networks, and Communications 2008. doi:10.1155/2008/583162.

Matthews, J.S.A., Vialet-Chabrand, S., Lawson, T., 2018. Acclimation to fluctuating light impacts the rapidity of response and diurnal rhythm of stomatal conductance. Plant Physiology 176, 1939–1951. doi:10.1104/pp.17.01809.

McAusland, L., Vialet-Chabrand, S., Davey, P., Baker, N.R., Brendel, O., Lawson, T., 2016. Effects of kinetics of light-induced stomatal responses on photosynthesis and water-use efficiency. New Phytologist 211, 1209–1220. doi:10.1111/nph.14000.

McKinney, W., 2010. Data structures for statistical computing in Python, in: Python in Science Conference, Austin, Texas. pp. 56–61. doi:10.25080/Majora-92bf1922-00a.

McKinney, W., 2011. Pandas: A foundational Python library for data analysis and statistics. Python for High Performance and Scientific Computing 14, 9.

Mir, R.R., Reynolds, M., Pinto, F., Khan, M.A., Bhat, M.A., 2019. High-throughput phenotyping for crop improvement in the genomics era. Plant Science 282, 60–72. doi:10.1016/j.plantsci.2019.01.007.

Murchie, E.H., Kefauver, S., Araus, J.L., Muller, O., Rascher, U., Flood, P.J., Lawson, T., 2018. Measuring the dynamic photosynthome. Annals of Botany 122, 207–220. doi:10.1093/aob/mcy087.

Murchie, E.H., Lawson, T., 2013. Chlorophyll fluorescence analysis: A guide to good practice and understanding some new applications. Journal of Experimental Botany 64, 3983–3998. doi:10.1093/jxb/ert208.

Murchie, E.H., Ruban, A.V., 2020. Dynamic non-photochemical quenching in plants: From molecular mechanism to productivity. The Plant Journal 101, 885–896. doi:10.1111/tpj.14601.

Okamoto, H., Lee, W.S., 2009. Green citrus detection using hyperspectral imaging. Computers and Electronics in Agriculture 66, 201–208. doi:10.1016/j.compag.2009.02.004.

Pedregosa, F., Varoquaux, G., Gramfort, A., Michel, V., Thirion, B., Grisel, O., Blondel, M., Prettenhofer, P., Weiss, R., Dubourg, V., Vanderplas, J., Passos, A., Cournapeau, D., Brucher, M., Perrot, M., Duchesnay, É., 2011. Scikit-Learn: Machine learning in Python. Journal of Machine Learning Research 12, 2825–2830.

Pieters, O., De Swaef, T., Lootens, P., Stock, M., Roldán-Ruiz, I., wyffels, F., 2020. Close range hyperspectral camera dataset with high temporal resolution of strawberry with eco-physiological data of one leaf. URL: https://doi.org/10.5281/zenodo.3897289, doi:10.5281/zenodo.3897289.

Rapaport, T., Hochberg, U., Shoshany, M., Karnieli, A., Rachmilevitch, S., 2015. Combining leaf physiology, hyperspectral imaging and partial least squares-regression (PLS-R) for grapevine water status assessment. ISPRS Journal of Photogrammetry and Remote Sensing 109, 88–97. doi:10.1016/j.isprsjprs.2015.09.003.

Rouse, J.W., Haas, R. H., Schell, J. A., Deering, D. W., 1974. Monitoring vegetation systems in the great plains with ERTS, in: Monitoring Vegetation Systems in the Great Plains with ERTS, pp. 309–317.

Salter, W.T., Merchant, A.M., Richards, R.A., Trethowan, R., Buckley, T.N., 2019. Rate of photosynthetic induction in fluctuating light varies widely among genotypes of wheat. Journal of Experimental Botany 70, 2787–2796. doi:10.1093/jxb/erz100.

Schurr, U., Walter, A., Rascher, U., 2006. Functional dynamics of plant growth and photosynthesis – from steady-state to dynamics – from homogeneity to heterogeneity. Plant, Cell & Environment 29, 340–352. doi:10.1111/j.1365-3040.2005.01490.x.

Shimadzu, S., Seo, M., Terashima, I., Yamori, W., 2019. Whole irradiated plant leaves showed faster photosynthetic induction than individually irradiated leaves via improved stomatal opening. Frontiers in Plant Science 10. doi:10.3389/fpls.2019.01512.

Silva-Perez, V., Molero, G., Serbin, S.P., Condon, A.G., Reynolds, M.P., Furbank, R.T., Evans, J.R., 2018. Hyperspectral reflectance as a tool to measure biochemical and physiological traits in wheat. Journal of Experimental Botany 69, 483–496. doi:10.1093/jxb/erx421.

Sims, D.A., Gamon, J.A., 2002. Relationships between leaf pigment content and spectral reflectance across a wide range of species, leaf structures and developmental stages. Remote Sensing of Environment 81, 337–354. doi:10.1016/S0034-4257(02)00010-X.

Tikhonov, A.N., 1963. On the solution of ill-posed problems and the method of regularization. Doklady Akademii Nauk SSSR 151, 501–504.

Townsend, A.J., Retkute, R., Chinnathambi, K., Randall, J.W.P., Foulkes, J., Carmo-Silva, E., Murchie, E.H., 2018. Suboptimal acclimation of photosynthesis to light in wheat canopies. Plant Physiology 176, 1233–1246. doi:10.1104/pp.17.01213.

Van De Vijver, R., Mertens, K., Heungens, K., Somers, B., Nuyttens, D., Borra-Serrano, I., Lootens, P., Roldán-Ruiz, I., Vangeyte, J., Saeys, W., 2020. In-field detection of *Alternaria solani* in potato crops using hyperspectral imaging. Computers and Electronics in Agriculture 168, 105106. doi:10.1016/j.compag.2019.105106.

Vialet-Chabrand, S., Matthews, J.S.A., Simkin, A.J., Raines, C.A., Lawson, T., 2017. Importance of fluctuations in light on plant photosynthetic acclimation. Plant Physiology 173, 2163–2179. doi:10.1104/pp.16.01767.

Vogelmann, J.E., Rock, B.N., Moss, D.M., 1993. Red edge spectral measurements from sugar maple leaves. International Journal of Remote Sensing 14, 1563–1575. doi:10.1080/01431169308953986.

Wahabzada, M., Mahlein, A.K., Bauckhage, C., Steiner, U., Oerke, E.C., Kersting, K., 2016. Plant phenotyping using probabilistic topic models: Uncovering the hyperspectral language of plants. Scientific Reports 6, 1–11. doi:10.1038/srep22482.

Weksler, S., Rozenstein, O., Haish, N., Moshelion, M., Walach, R., Ben-Dor, E., 2020. A hyperspectral-physiological phenomics system: Measuring diurnal transpiration rates and diurnal reflectance. Remote Sensing 12, 1493. doi:10.3390/rs12091493.

Yendrek, C.R., Tomaz, T., Montes, C.M., Cao, Y., Morse, A.M., Brown, P.J., McIntyre, L.M., Leakey, A.D.B., Ainsworth, E.A., 2017. High-throughput phenotyping of maize leaf physiological and biochemical traits using hyperspectral reflectance. Plant Physiology 173, 614–626. doi:10.1104/pp.16.01447.

Zarco-Tejada, P.J., Catalina, A., González, M.R., Martín, P., 2013a. Relationships between net photosynthesis and steady-state chlorophyll fluorescence retrieved from airborne hyperspectral imagery. Remote Sensing of Environment 136, 247–258. doi:10.1016/j.rse.2013.05.011.

Zarco-Tejada, P.J., Morales, A., Testi, L., Villalobos, F.J., 2013b. Spatio-temporal patterns of chlorophyll fluorescence and physiological and structural indices acquired from hyperspectral imagery as compared with carbon fluxes measured with eddy covariance. Remote Sensing of Environment 133, 102–115. doi:10.1016/j.rse.2013.02.003.

Zhao, D., Reddy, K.R., Kakani, V.G., Reddy, V.R., 2005. Nitrogen deficiency effects on plant growth, leaf photosynthesis, and hyperspectral reflectance properties of sorghum. European Journal of Agronomy 22, 391–403. doi:10.1016/j.eja.2004.06.005.

6. Author contributions statement (CRediT)

Olivier Pieters	Conceptualization, Methodology, Data curation, Software, Validation, Investigation, Writing - original draft, Writing - review & editing, Visualization
Tom De Swaef	Conceptualization, Methodology, Writing - original draft, Writing - review & editing
Peter Lootens	Conceptualization, Methodology, Writing - review & editing
Michiel Stock	Conceptualization, Methodology, Writing - review & editing
Isabel Roldán-Ruiz	Conceptualization, Methodology, Writing - review & editing
Francis wyffels	Conceptualization, Methodology, Writing - review & editing

7. Conflicts of Interest

The authors declare no conflict of interest.

8. Supplementary Materials

8.1. Additional Tables and Figures for the Analysis

856 (6.9)	867 (8.4)	846 (7.9)	834 (10.6)	953 (21.5)
937 (19.7)	945 (16.9)	929 (16.1)	920 (15.0)	960 (15.5)
750 (6.3)	765 (6.6)	738 (4.7)	724 (5.2)	699 (4.1)
803 (7.5)	815 (7.5)	790 (9.4)	777 (6.8)	684 (4.4)
897 (13.2)	907 (13.3)	887 (13.0)	876 (12.0)	678 (3.1)

Table 3: Hyperspectral pixel, represented as physical 2D-grid of peak bands in nm and width half-peak-full-width specified between brackets in nm of the near-infrared sensor (H1).

538 (12.9)	552 (13.0)	524 (9.2)	512 (6.5)
620 (5.1)	480 (6.6)	611 (12.2)	602 (12.1)
580 (10.7)	591 (11.4)	567 (11.0)	554 (11.7)
489 (10.6)	500 (8.2)	477 (7.9)	470 (2.9)

Table 4: Hyperspectral pixel, represented as physical 2D-grid of peak bands in nm and width half-peak-full-width specified between brackets in nm of the visual sensor (H2).

For reference, tables are included that depict exact numbers instead of bar charts. Table 5 corresponds to fig. 6, while table 6 matches fig. 9

8.2. Shutter time and Gain Compensation Details

The shutter time and gain values are automatically determined by the camera to achieve higher dynamic range, especially in low-light conditions. Consequently, the resulting image data have to be rescaled to the same scale. This is done using the following transformation:

$$q = \frac{p}{r_c(s - x_0) + y_0} \tag{4}$$

Where q is the transformed version of pixel value p, with shutter time s. The other values depend upon the camera used and gain setting. The values are listed in table 7. These were obtained by maintaining the same light intensity, while varying and camera configuration. Transforming these using eq. (4), results in a constant value.

Table 5: Performance of the linear model for different eco-physiological and environmental parameters. The lower the NMSE, the better. ~~VI~~ means that the model was trained without the vegetation indices (VI), while VI indicates that they were included. This table provides the same information as fig. 6, but in a different form.

task	plant1		plant2		wood		PVC		Ytong		cotton	
	~~VI~~	VI	~~VI~~	VI	~~VI~~	VI	~~VI~~	VI	~~VI~~	VI	~~VI~~	VI
P_n	0.301	0.206	0.556	0.56	0.523	0.34	0.395	0.34	0.585	0.625	0.589	0.587
g_s	0.676	0.653	0.958	0.957	0.913	0.634	0.693	0.649	0.977	1.006	0.99	1.002
Tr	0.426	0.408	0.597	0.602	0.5	0.309	0.4	0.353	0.647	0.656	0.656	0.646
VPD_{leaf}	0.18	0.107	0.277	0.233	0.214	0.135	0.201	0.156	0.285	0.252	0.31	0.277
T_{leaf}	0.052	0.027	0.07	0.035	0.052	0.034	0.064	0.031	0.092	0.048	0.088	0.041
T_{air}	0.081	0.02	0.068	0.044	0.134	0.124	0.164	0.1	0.121	0.075	0.109	0.062
RH	0.432	0.297	0.382	0.439	0.478	0.371	0.466	0.436	0.631	1.132	0.356	0.325
PAR	0.025	0.018	0.03	0.039	0.024	0.016	0.021	0.015	0.029	0.03	0.028	0.027

Table 6: Overview of performance for all variables for a subsample size of 77 (30+47), resulting in 1502 input features for the model. Mean ($\bar{y}$) and standard deviation (σ) columns provide the same information as fig. 9 in table form.

task	plant1		plant2		wood		PVC		Ytong		cotton	
	$\bar{y}$	σ	$\bar{y}$	σ	$\bar{y}$	σ	$\bar{y}$	σ	$\bar{y}$	σ	$\bar{y}$	σ
P_n	0.262	0.039	0.574	0.039	0.271	0.032	0.282	0.029	0.55	0.011	0.544	0.014
g_s	0.613	0.046	0.854	0.046	0.668	0.023	0.701	0.022	0.923	0.008	0.914	0.015
Tr	0.451	0.04	0.51	0.032	0.411	0.008	0.419	0.014	0.637	0.01	0.671	0.011
VPD_{leaf}	0.217	0.035	0.352	0.019	0.222	0.009	0.217	0.012	0.349	0.006	0.402	0.024
T_{leaf}	0.057	0.01	0.138	0.041	0.052	0.003	0.066	0.001	0.115	0.019	0.109	0.004
T_{air}	0.11	0.028	0.151	0.048	0.103	0.015	0.101	0.007	0.159	0.03	0.142	0.005
RH	0.432	0.066	0.684	0.125	0.421	0.038	0.32	0.023	0.616	0.04	0.574	0.022
PAR	0.026	0.001	0.028	0.001	0.02	0	0.022	0	0.026	0	0.027	0

camera	gain	r_c	x_0	y_0
NIR	0	0.1216	7,200	1,454
NIR	12	0.1216	7,200	3,478
VIS	0	0.1301	7,200	2,213
VIS	12	0.1301	7,200	4,004

Table 7: Correction values for shutter time and gain compensation.

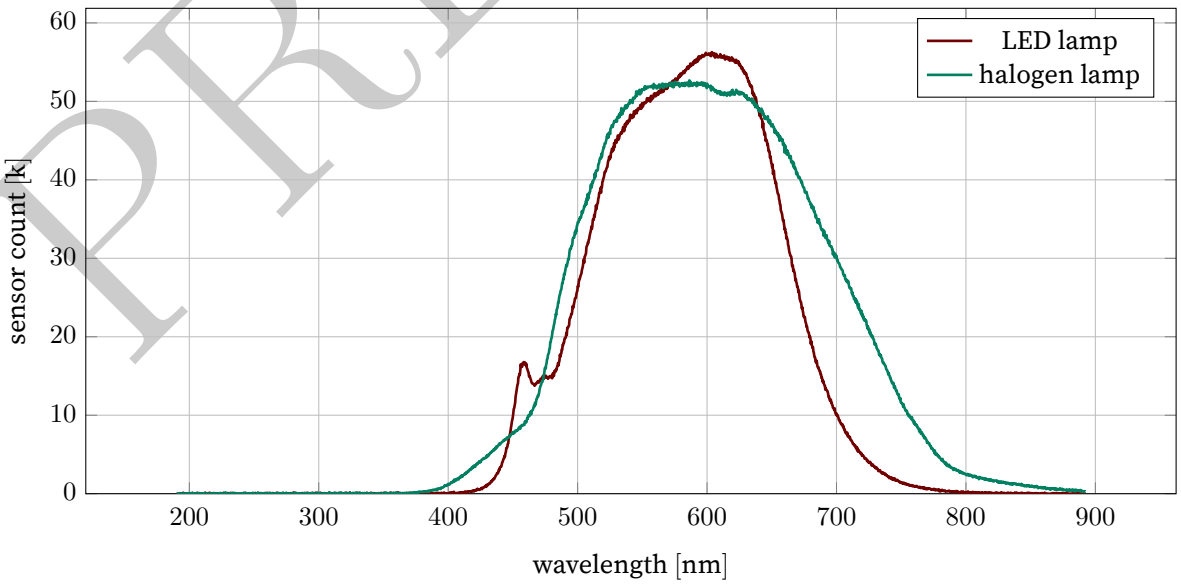

Figure 11: Spectrum of the halogen lights and LED lights used in the experiments. The spectral were measured using Jaz Spectrometer (Ocean Optics, Dunedin, FL, USA) from a distance of 20 cm directly below the light source.

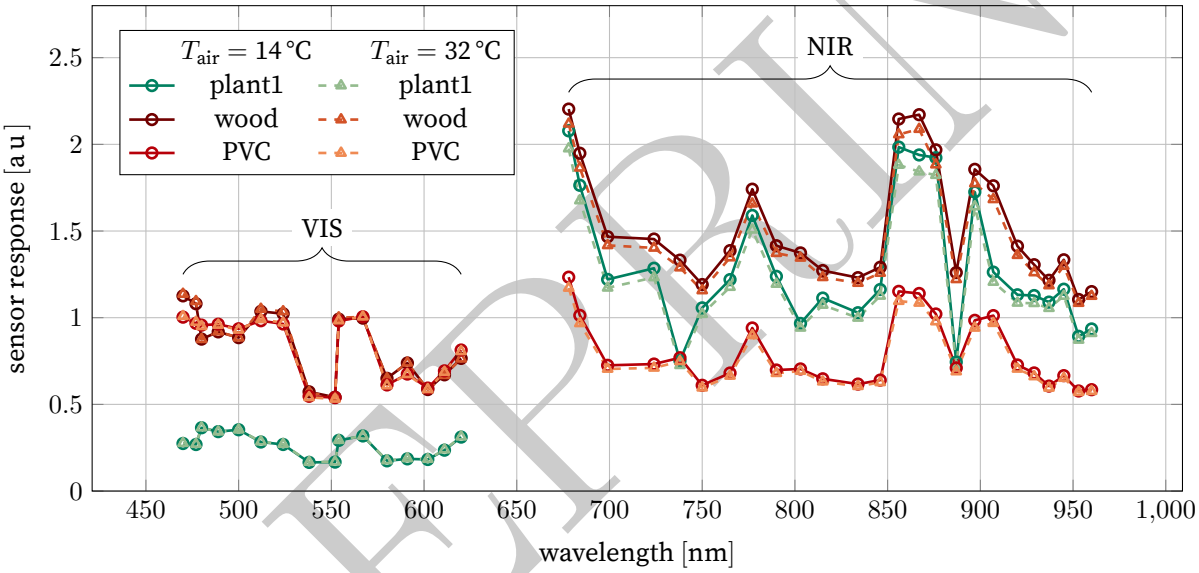

Figure 12: Reflection spectra of the three materials in the first experiments at similar PAR conditions ($200\,\mu mol\,m^{-2}\,s^{-1}$) at two different temperatures, $T_{air} = 14\,°C$ and $T_{air} = 32\,°C$, illustrating the variable spectral response. The peaking of some peaks is the result of strong secondary peaks of the sensor's response and the emission spectra of the lights, depicted in fig. 11.